Effect of Al³⁺ substitution on structural, morphological, magnetic, optical, and functional study of ZnFe₂O₄ nanoparticles

M. Sundararajan ✉ ⓘ ; Kholod Dahlous; M. Ramesh ⓘ ; R. S. Rimal Isaac; S. Yuvaraj ✉ ⓘ ;
Jothi Ramalingam Rajabathar ⓘ ; Chandra Sekhar Dash ⓘ ; P. Aji Udhaya ⓘ

Check for updates

View Online   Export Citation

Articles You May Be Interested In

X-ray diffraction and Raman scattering study of Cr-doped ZnFe₂O₄ spinel ferrites

AIP Conference Proceedings (June 2015)

Synthesis, characterization and conductivity studies of ZnFe₂O₄ nanoparticles

AIP Conference Proceedings (June 2015)

Poly (vinyl pyrrolidone) as a capping of synthesized powdered MgFe₂O₄@ZnFe₂O₄ nanocomposite ferrite by microwave-assisted combustion method

AIP Conference Proceedings (August 2022)

Effect of Al³⁺ substitution on structural, morphological, magnetic, optical, and functional study of ZnFe₂O₄ nanoparticles

M. Sundararajan,[1,2,a] (ID) Kholod Dahlous,[3] M. Ramesh,[4] (ID) R. S. Rimal Isaac,[5] S. Yuvaraj,[6,a] (ID)
Jothi Ramalingam Rajabathar,[3,b] (ID) Chandra Sekhar Dash,[7] (ID) and P. Aji Udhaya[8] (ID)

AFFILIATIONS

[1] PG and Research Department of Physics, Paavendhar College of Arts and Science, M. V. South, Thalaivasal, Salem, Tamil Nadu 636 121, India

[2] Department of Chemistry, Korea Advanced Institute of Science and Technology, Daejeon 34141, South Korea

[3] Department of Chemistry, College of Science, King Saud University, P.O.Box 2455, Riyadh 11451, Saudi Arabia

[4] Department of Chemistry, Vel Tech Rangarajan Dr. Sagunthala R&D Institute of Science and Technology, Vel Nagar, Avadi, Chennai 600 062, Tamil Nadu, India

[5] Department of Nanotechnology, Noorul Islam Centre for Higher Education, Kumaracoil, Kanyakumari 629180, Tamilnadu, India

[6] Department of Physics, Vel Tech Rangarajan Dr. Sagunthala R&D Institute of Science and Technology, Vel Nagar, Avadi, Chennai 600 062, Tamil Nadu, India

[7] Department of Electronics and Communication Engineering, Centurion University of Technology and Management, Odisha, Bhubaneswar 752050, India

[8] Department of Physics, Holy Cross College, Nagercoil 629004, Tamil Nadu, India

[a] Authors to whom correspondence should be addressed: sundar15msc@gmail.com and phyuvaraj@gmail.com
[b] jrajabathar@ksu.edu.sa

ABSTRACT

ZnFe$_{1-x}$Al$_x$O$_4$ (x = 0.0, 0.1, 0.3, and 0.5) samples were synthesized by the combustion method. The x-ray diffraction pattern confirms that the ferrite samples have a cubic inverse spinel structure, and Rietveld refinement adds more weight to this conclusion. Furthermore, the space group is $Fd\bar{3}m$. Using Rietveld analysis, the oxygen location, lattice parameter, and cation distribution were found, proving that Al doped ZnFe$_2$O$_4$ ferrites were present in every sample. According to structural research, when the Al^{3+} concentration increases, the crystallite size decreases (15–29 nm) but the lattice parameter increases (8.399–8.418 Å). The FE-SEM images are agglomerated for all the ferrite samples. The estimated energy gap (1.83–2.05 eV) increases as the doping concentration is increased. The FT-IR spectrum revealed the formation of Al doped ZnFe$_2$O$_4$ nanoparticles, and vibrating sample magnetometry showed the ferromagnetic behavior.

I. INTRODUCTION

A class of magnetic iron oxides known as ferrites have a cubic spinel structure and are generally expressed by the formula AB$_2$O$_4$. These compounds have a nearly perfect cubic close-packed structure, with oxygen atoms arranged in an ideal manner. Within this structure, there are eight tetrahedral sites (A-sites) and 16 octahedral sites (B-sites) occupied by Fe^{2+} ions. The 16 B-sites include an equal distribution of Fe^{2+} and Fe^{3+} ions.[1] When a divalent transition metal ion replaces another ion in the tetrahedral location, the ferrite displays a characteristic normal spinel structure. In contrast, the formation of an inverted spinel structure occurs when the divalent transition metal is present at the octahedral position. A more complex situation arises when divalent transition metal ions are added to both the A and B sublattices; this usually leads to a mixed or disordered structure. Recent research has placed growing

emphasis on examining both large-scale ferrite samples and tiny crystals at the nanoscale, specifically to investigate their distinct magnetic properties and possible uses.[2]

The distribution of cations among octahedral (B) and tetrahedral (A) sites plays a crucial role in defining the magnetic and structural properties of ferrites, especially when replacements exist at the Fe sites. Zinc ferrite, or $ZnFe_2O_4$, has a distinctive spinel structure where all ferric ions occupy the octahedral sites and Zn^{2+} ions occupy the tetrahedral sites because of their propensity to form sp^3 bonds with oxygen anions. The specific arrangement of cations in zinc ferrite results in its distinctive low Néel temperature and weak superexchange interaction. These properties are controlled by the 90° bond angle between Fe^{3+} and O^- ions, causing $ZnFe_2O_4$ to exhibit paramagnetic behavior at ambient temperature.[3] Furthermore, it has been proposed that the distribution of cations between the octahedral and tetrahedral sites in Mn-doped $ZnFe_2O_4$ is random.[4] Technically speaking, spinel-containing zinc ferrites are extremely valuable because of their many applications in fields such as electronics, drug delivery systems, medical diagnostics, information storage, and magnetic resonance imaging (MRI) contrast agents. Obtaining particles with a precise and limited range of sizes is essential for tackling a range of technological obstacles. Precise manipulation of particle size is crucial in doped ferrites as it influences the tendency of electrons to concentrate at the interfaces of nanostructured substances. By localizing, the eddy current losses in electrical applications are reduced, making these materials particularly ideal for use as cores in inductive components that operate at high frequencies. $ZnFe_{1-x}Al_xO_4$ (where x = 0.0, 0.1, 0.3, and 0.5) ferrites exhibit unique superparamagnetic properties due to their nanoscale, single-domain structure.[5] Several synthesis methods have been developed and reported in the literature for the production of magnetic nanoparticles, including spray pyrolysis, hydrothermal preparation, microemulsion methods, and microwave irradiation of ferrous hydroxide.[6–10]

The co-precipitation method offers the advantage of being relatively simple while allowing for effective control over the particle properties. Although there is extensive research on the structural characteristics of $ZnFe_{1-x}Al_xO_4$ (x = 0.0–0.5) ferrites, there remains limited information on aspects such as synthesis temperature, site occupancy, and cation ordering. To explore these factors, $ZnFe_{1-x}Al_xO_4$ ferrites have been synthesized using the chemical co-precipitation technique, aiming to investigate their structural, vibrational, and magnetic properties. This series of $ZnFe_{1-x}Al_xO_4$ (x = 0.0, 0.1, 0.3, and 0.5) ferrites has been thoroughly characterized using various techniques, including FT-IR, Rietveld analysis, VSM (vibrating sample magnetometry), DRS-UV, FESEM (field emission scanning electron microscopy), EDX (energy-dispersive x-ray spectroscopy), and XRD (x-ray diffraction) spectroscopy.

II. EXPERIMENTAL

A. Chemicals

Aluminum doped zinc ferrite nanoparticles [$Zn(NO_3)_2 \cdot 6H_2O$, $Al(NO_3)_3 \cdot 9H_2O$, $Fe(NO_3)_3 \cdot 9H_2O$, and L arginine] were obtained from Merck and employed in the synthesis of zinc ferrite. Every chemical utilized was of AR grade and did not require any additional purification. All of the trials' water was distilled to have a lower conductivity.

B. $ZnFe_{1-x}Al_xO_4$ (x = 0.0, 0.1, 0.3, and 0.5) preparation

The combustion method was used to create $ZnFe_{1-x}Al_xO_4$ (x = 0.0–0.5) particles. $Zn(NO_3)_2 \cdot 6H_2O$, $Al(NO_3)_3 \cdot 9H_2O$, $Fe(NO_3)_3 \cdot 9H_2O$, and L arginine were freshly made in proper mole ratios (1:2). To prepare the Al-doped $ZnFe_2O_4$ samples, a solution of L-arginine was added to the precursor solutions and stirred vigorously for one hour. The nitrate precursors serve as oxidizers in this process, while L-arginine serves as the fuel. The well-mixed homogeneous solution was then transferred to a 250 ml beaker and heated at 90 °C for 20 min. During this heating, the solution was first boiled, followed by vaporization and dehydration, which eventually led to the breakdown of the solution and the release of reaction gases. Following a series of events, the Al-doped $ZnFe_2O_4$ material was quickly produced through spontaneous ignition. The resulting samples were then washed thoroughly with distilled water and ethanol. After washing, the samples were subjected to calcination, where the temperature was increased to 570 °C and maintained for 90 min. To distinguish them from one another, the samples were then given the labels a, b, c, and d, respectively.

C. Characterization

Utilizing CuKα (λ = 1.5406 A) radiation from 20° to 80°, a Siefert 3003T/T x-ray diffractometer was used to study the phase development and crystal structure. Using an EDAX detector, an FEI Quanta FEG 200 scanning electron microscope was used to examine the surface morphology. Using a twin beam PerkinElmer (Lambda 35) spectrophotometer, UV-visible absorption spectra were obtained between 200 and 800 nm. The FTIR spectra (400–4000 cm^{-1}) were obtained for these studies using an FT-IR-PerkinElmer Spectrum RX 1 model. Using a Lake Shore model 7404 with three magnets, the VSM analysis was successfully completed by an RT HIOKI 3532-50 LCR. Utilizing a Hitester and Keithley 6514 electrometer, the electrical characteristics of the materials were examined.

III. RESULTS AND DISCUSSION

A. XRD analysis

The Al doped $ZnFe_2O_4$ samples' x-ray diffraction (XRD) patterns are displayed in Fig. 1. The peaks at 30.82, 36.61, 43.19, 54.10, 56.92, 62.54, and 73.49 correspond to the (220), (311), (400), (422), (511), (440), and (533) planes of $ZnFe_2O_4$ nanoparticles. The pattern verified a multiphase, crystalline structure free of any peaks associated with impurities. Based on the JCPDS card number 22-1012, the peaks were indexed to the cubic $ZnFe_2O_4$ phase. The extra peaks belong to Fe_2O_3 nanoparticles.[11,12]

As the Al concentration in the samples increases, it was discovered that the lattice constant value increases. In good accordance with previously reported values of 0.8330 and 0.8435 Å, the lattice parameters of $ZnFe_2O_4$ nanoparticles were found to be a = 0.8399 Å and a = 0.8418 Å, respectively. The regular spinel structure undergoes crystal lattice contraction as Al^{3+} (ion radius 1.42 Å) ions replace Fe^{3+} (ion radius 0.76 Å) ions.[13]

Fullprof software was used to carry out the Rietveld refinements for the Al-doped $ZnFe_2O_4$ samples; the outcomes are shown in Fig. 2. To validate the formation of two distinct phases, these refinements were made. Both the simulated and observed x-ray diffraction
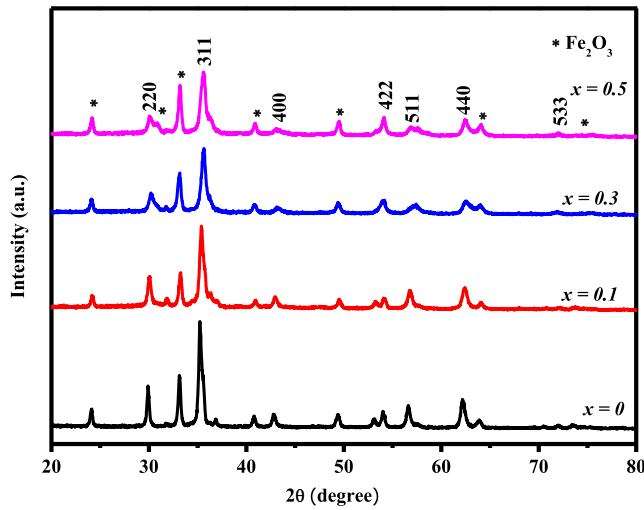
FIG. 1. XRD pattern of $ZnFe_{1-x}Al_xO_4$ (x = 0.0, 0.1, 0.3, and 0.5) nanoparticles.

patterns of the Al-doped $ZnFe_2O_4$ nanoparticles show a strong correlation [Figs. 2(a)–2(d)]. Furthermore, the values shown in Table I, which are close to unity, indicate a high degree of accuracy between the observed and calculated 2θ values. The weighted profile factor (called Rwp) and the expected weighted profile reliability factor (called Re) are used to calculate the parameter "S," which measures the goodness of fit. The refined parameters are estimated with high accuracy when the "S" value is close to unity, which indicates an excellent fit between the observed data and the model.[14]

B. Morphology study

FE-SEM micrographs are shown in Figs. 3(a)–3(d). These samples exhibit spherical morphology as well, with a consistent diameter of roughly 20 nm. Through manipulation of the growth parameters, including temperature and reaction time, as well as the starting concentration, the diameter of these Al doped $ZnFe_2O_4$ microspheres may be controlled to be between 15 and 29 nm. The transition from discrete particles to an agglomerated texture with
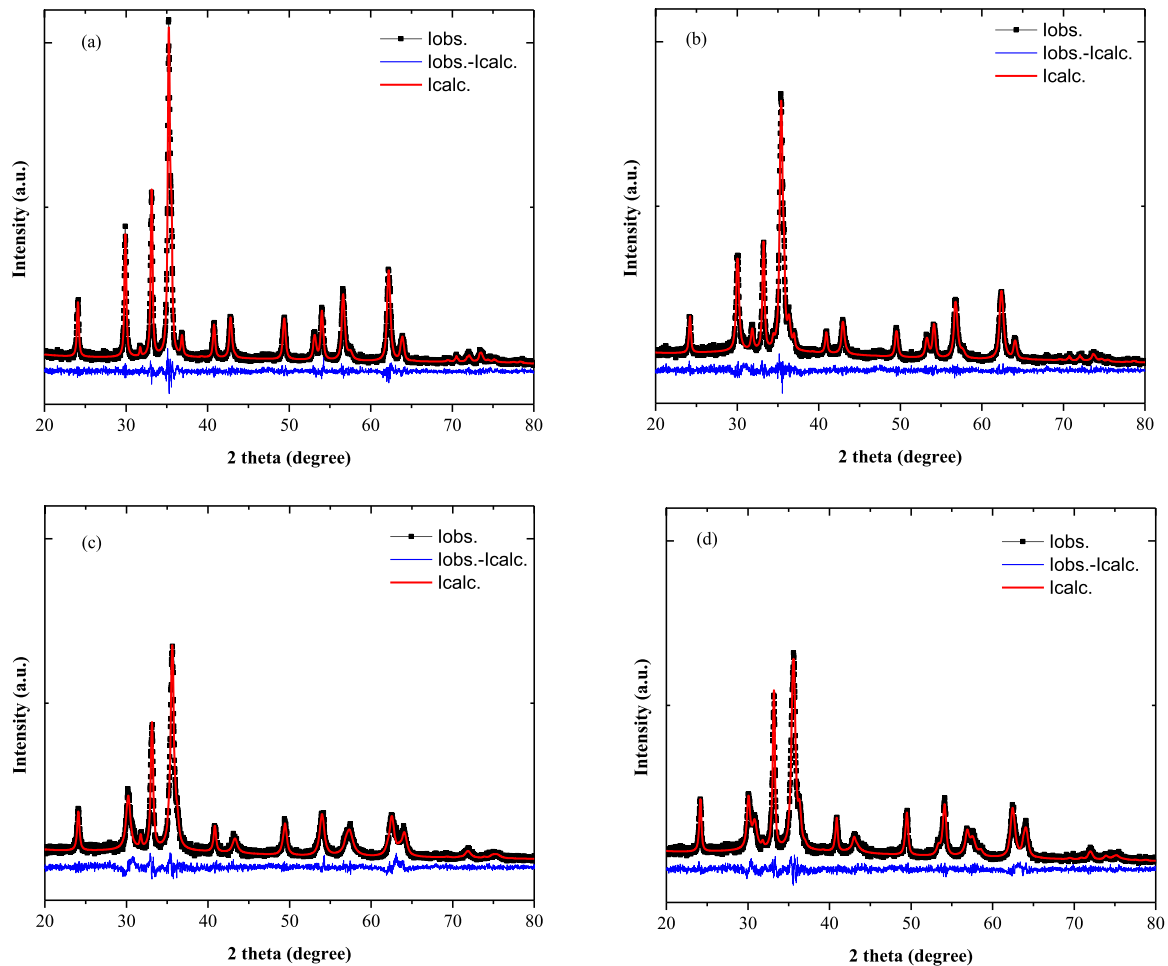

FIG. 2. Rietveld analysis of (a) $ZnFe_2O_4$, (b) $ZnFe_{0.9}Al_{0.1}O_4$, (c) $ZnFe_{0.7}Al_{0.3}O_4$, and (d) $ZnFe_{0.5}Al_{0.5}O_4$ nanoparticles.

TABLE I. Sample code, crystallite size, lattice parameter, Rietveld refinement factors, and bandgap values of $ZnFe_{2-x}Al_xO_4$ (x = 0.0, 0.1, 0.3, and 0.5) samples.

Sample	Sample code	Crystallite size, L (nm)	Lattice parameter, a = b = c (Å)	Fit parameters	Energy gap (eV)
$ZnFe_2O_4$	a	15	8.399	R_{wp} = 4.38 R_p = 3.61 R_e = 3.97 S = 1.10	1.83
$ZnFe_{1.9}Al_{0.1}$ Fe_2O_4	b	19	8.404	R_{wp} = 9.53 R_p = 7.43 R_e = 8.63 S = 1.11	1.86
$ZnFe_{1.7}Al_{0.3}$ Fe_2O_4	c	24	8.411	R_{wp} = 12.35 R_p = 6.35 R_e = 9.91 S = 1.25	1.97
$ZnFe_{1.5}Al_{0.5}$ Fe_2O_4	d	29	8.418	R_{wp} = 11.20 R_p = 8.87 R_e = 9.70 S = 1.16	2.05
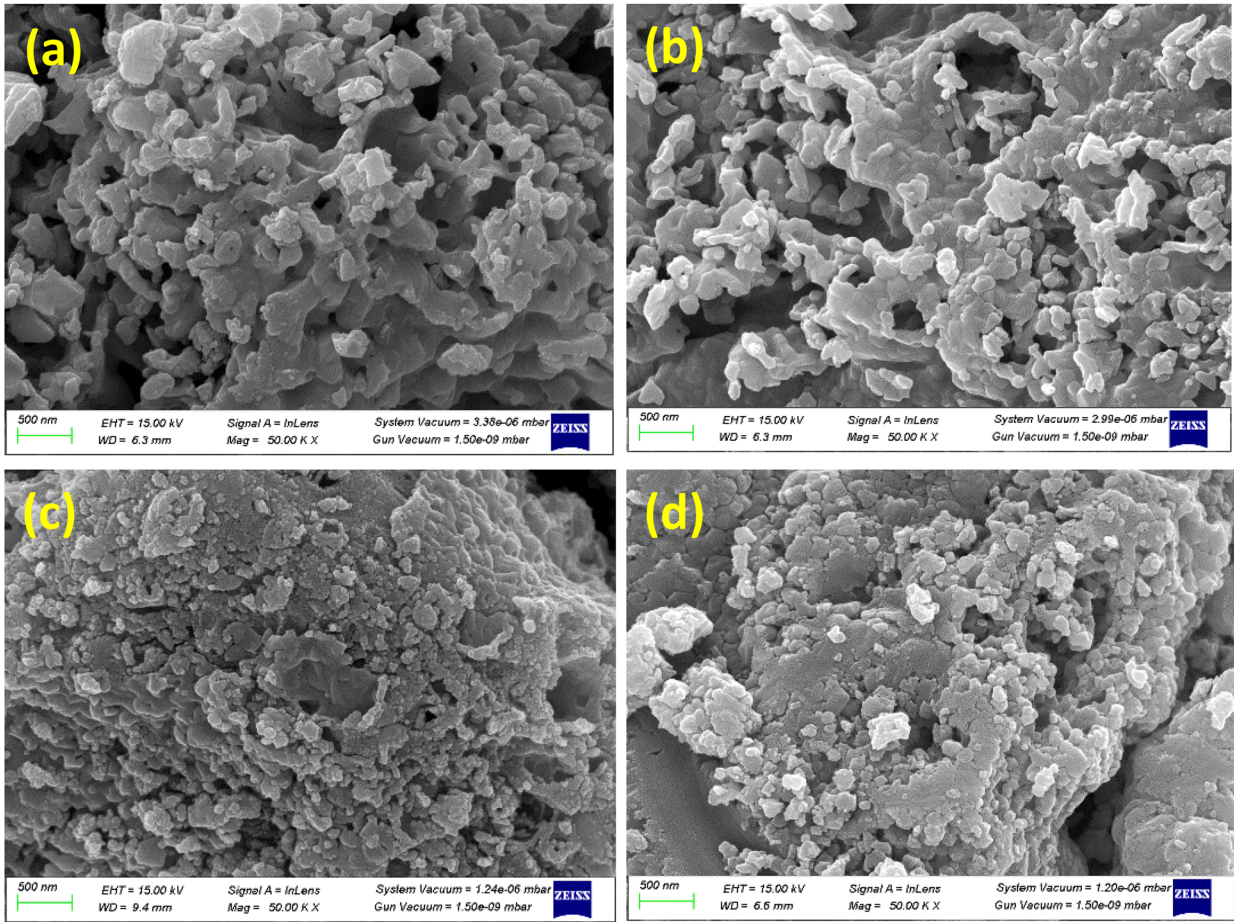
FIG. 3. FESEM image of (a) $ZnFe_2O_4$, (b) $ZnFe_{0.9}Al_{0.1}O_4$, (c) $ZnFe_{0.7}Al_{0.3}O_4$, and (d) $ZnFe_{0.5}Al_{0.5}O_4$ nanoparticles.

increasing Al doping is attributed to the influence of Al^{3+} ions on the growth and crystallization process, as well as the increased surface energy promoting particle clustering. To control morphology across all samples, various parameters can be optimized, such as synthesis temperature and reaction time, which can influence particle growth and prevent agglomeration. Limiting the doping concentration of Al^{3+} to a lower range may help preserve the particle morphology, and gentle post-synthesis treatments, such as careful drying or annealing, can further minimize clustering. A systematic approach to fine-tuning these parameters could ensure morphology control while maintaining the functional properties of the Al-doped $ZnFe_2O_4$ nanoparticles.

The chemical makeup of the as-prepared ferrite products was ascertained by the utilization of energy dispersive x-ray analysis. EDAX spectra obtained from individual as-prepared ferrite microspheres revealed that samples for Al doped $ZnFe_2O_4$ exclusively contained Al, Zn, Fe, and O [Figs. 4(a)–4(d)]. In addition, the inset table images shown in Figs. 4(a)–4(d) confirmed the elemental composition of the treated sample by showing the presence of Zn, Al, Fe, and O atoms.

C. Bandgap studies

By examining the UV-visible diffuse reflectance spectra of the Al doped $ZnFe_2O_4$ samples between 200 and 800 nm in wavelength, the optical properties of the samples were examined. Diffuse reflectance studies were utilized to determine the energy of the optical bandgap (Eg). The revised Tau-c connection equation was employed to ascertain the Eg value using the following equation:

$$\alpha h\nu = A(h\nu - E_g)^n, \tag{1}$$
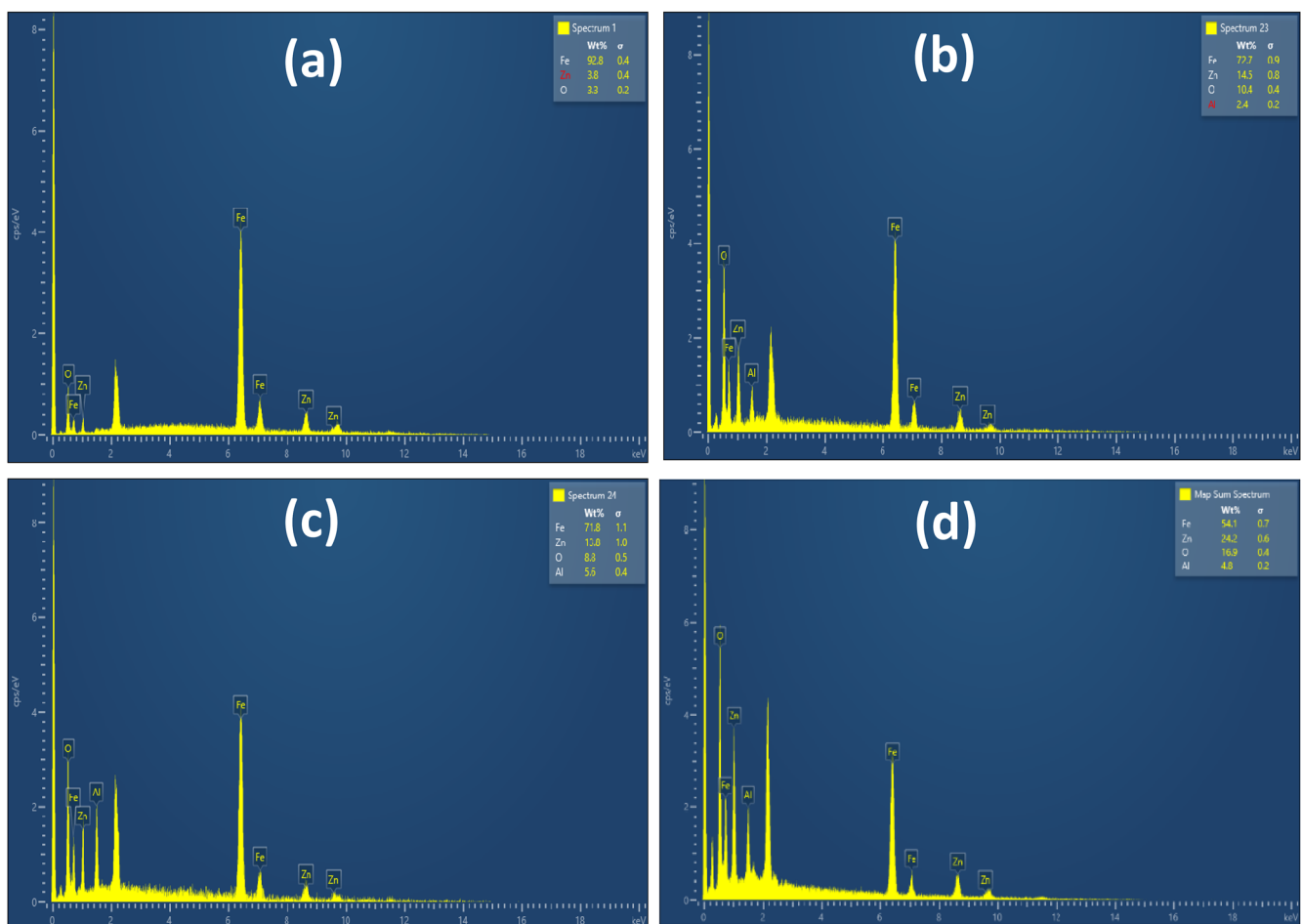
$$\alpha = F(R) = \frac{(1-R)^2}{2R}. \tag{2}$$

FIG. 4. EDX of (a) $ZnFe_2O_4$, (b) $ZnFe_{0.9}Al_{0.1}O_4$, (c) $ZnFe_{0.7}Al_{0.3}O_4$, and (d) $ZnFe_{0.5}Al_{0.5}O_4$ nanoparticles.

In this particular situation, the term [F(R)] corresponds to the Kubelka–Munk function [Eq. (2)], where α represents the coefficient for photon absorption and R denotes the reflectance. A graph is created with hν displayed on the horizontal axis and $[F(R)h\nu]^2$ represented on the vertical axis in order to investigate the correlation between these variables. The direct bandgap values are shown in Figs. 5(a)–5(d), and they are obtained by extending these graphs' linear sections to the point where $[F(R)h\nu]^2$ reaches zero. This extrapolation allows for the estimation of the bandgap energy values. The calculated bandgap energies for the compositions x = 0, 0.1, 0.3, and 0.5 are 1.83, 1.86, 1.97, and 2.05 eV, respectively. The quantum confinement effect in the nanoscale regime is responsible for the higher bandgap value of 2.03 eV found in pure zinc ferrite. The optical bandgap values progressively decrease as the aluminum concentration increases. When a material's dimensions approach the nanoscale, which is usually less than 100 nm, quantum confinement effects become more apparent.[15]

D. FT-IR analysis

Figures 6(a)–6(d) display the Fourier-transform infrared (FT-IR) spectra of Al doped $ZnFe_2O_4$ samples obtained by the combustion process. The O-H functional group of water molecules was identified as the source of the broad spectral band seen at 3441 cm^{-1}. The O-H bonds are attributed to the transition band at 2917 and 2851 cm^{-1}. The H-O-H bond is responsible for the bands seen at 1641 and 1416 cm^{-1}, respectively. The remaining nitrogen groups are responsible for a noticeable peak at 1322 cm^{-1}, which may be the consequence of the specific combustion technique employed.[16] The bands seen at 1059, 778, 544, and 450 cm^{-1} correspond to the
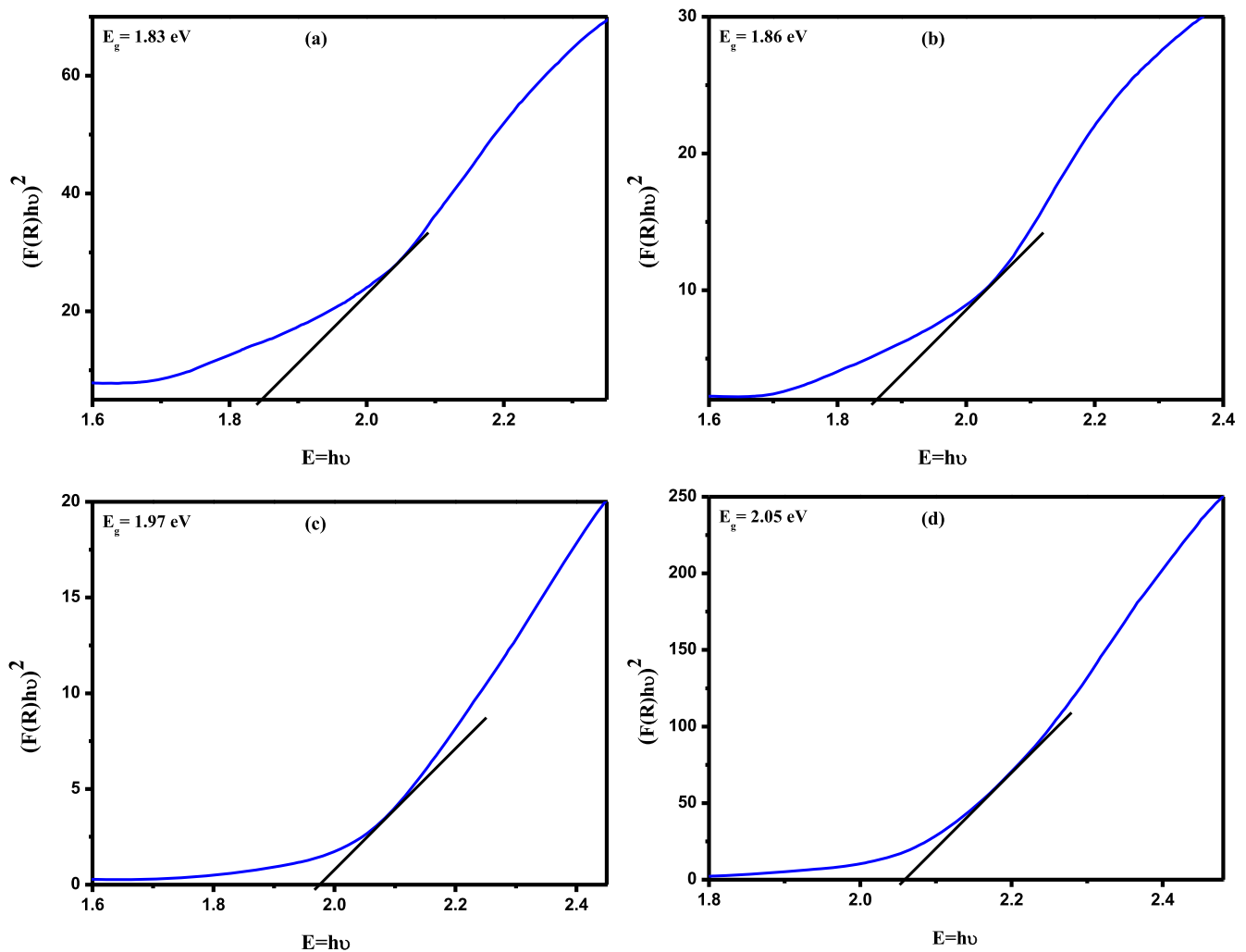

FIG. 5. Energy gap of (a) $ZnFe_2O_4$, (b) $ZnFe_{0.9}Al_{0.1}O_4$, (c) $ZnFe_{0.7}Al_{0.3}O_4$, and (d) $ZnFe_{0.5}Al_{0.5}O_4$ nanoparticles.
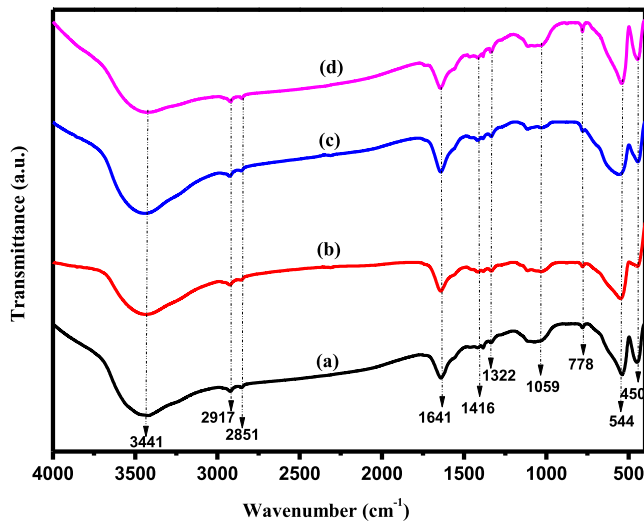
FIG. 6. FTIR of (a) $ZnFe_2O_4$, (b) $ZnFe_{0.9}Al_{0.1}O_4$, (c) $ZnFe_{0.7}Al_{0.3}O_4$, and (d) $ZnFe_{0.5}Al_{0.5}O_4$ nanoparticles.

presence of octahedral group complexes of $Zn^{2+}-O^{2-}$ and $Fe^{3+}-O^{2-}$ at tetrahedral sites in the zinc ferrite nanoparticles, respectively.

E. VSM analysis

The ferromagnetic properties of the Al-doped $ZnFe_2O_4$ samples are demonstrated by the hysteresis curve of the magnetization-field (M-H) in Figs. 7(a)–7(d). Both positive and negative values, ranging from +15 to −15 kOe, are included in the range of the magnetic field studied at room temperature (Table II). In the Al^3-doped $ZnFe_2O_4$ system, the magnetic saturation (Ms) values range from 3.056 to 12.62 emu/g, while the remanent magnetization (Mr)

FIG. 7. VSM spectra of (a) $ZnFe_2O_4$, (b) $ZnFe_{0.9}Al_{0.1}O_4$, (c) $ZnFe_{0.7}Al_{0.3}O_4$, and (d) $ZnFe_{0.5}Al_{0.5}O_4$ nanoparticles.

values range from 0.71 to 2.25 emu/g, corresponding to different Al^{3+} concentrations (x = 0–0.5). It is observed that the coercivity (Hc) values vary between 294.75 and 95.22 Oe. As a result, variations in magnetic characteristics such as remanent magnetization (Mr), saturation magnetization (M_s), and coercivity (H_c) can provide important information about a material's magnetic behavior. In general, a material's magnetic behavior can be impacted by the addition of impurities or dopant atoms. It is possible for some dopants, such as aluminum ions, to decrease the total saturation magnetization while increasing coercivity. An increase in coercivity (Hc) suggests that the material's magnetic domains are becoming more resistant to alignment or reversal. This may be explained by elements such as elevated magnetic anisotropy, defect concentration, or structural alterations, such as a shift from normal to inverse spinel. As the difficulty of reorienting domains increases, the remanent magnetization (Mr) of the material may decrease. In this context, the size and shape of the nanoparticles play a crucial role in determining their magnetic properties. When a material is nanostructured, it may exhibit an increase in Hc along with a decrease in Ms (magnetic saturation) and Mr (magnetic remanence). These alterations are frequently the result of amplified surface effects or quantum size effects. Doped samples have a lower crystalline size than pure $ZnFe_2O_4$, indicating a higher fraction of surface atoms. This can dramatically affect their magnetic behavior.[17–20]

F. Dielectric studies

The effects of frequency and temperature on the conductivity properties of $ZnFe_2O_4$ nanoparticles doped with Al are investigated through the use of dielectric analysis. The ability to perceive a material's polarizabilities at a certain frequency is crucial for understanding its dielectric characteristics. Figures 8(a)–8(d) display the dielectric constant of Al doped $ZnFe_2O_4$ NPs with temperature and frequency fluctuations using the following equation:

$$\varepsilon_r = CD/\varepsilon_0 A, \qquad (3)$$

where C is the capacitance of the parallel plate capacitor, A is its area, D is its thickness, and λ is the permittivity of empty space. Every sample exhibits a discernible pattern wherein the dielectric constant (εr) progressively decreases with an increase in frequency. At low applied field frequency, the dipoles in the sample oscillate in response to the external field. When polarization reaches saturation, dipoles respond to the external field by slightly altering the value of the dielectric constant, ε_r.[21] As the Al molar ratio increases, the dielectric constant also increases. This is because the development of additional defect levels in the Al doped $ZnFe_2O_4$ nanoparticles enhances their polar centers.[22]

G. AC conductivity

We can gain a better grasp of charge carrier movement by studying AC conductivity. The AC conductivity of spinel nanoparticles doped with varying concentrations of Al-doped $ZnFe_2O_4$ was measured. Using the following equation, the electrical conductivity of the material was determined:

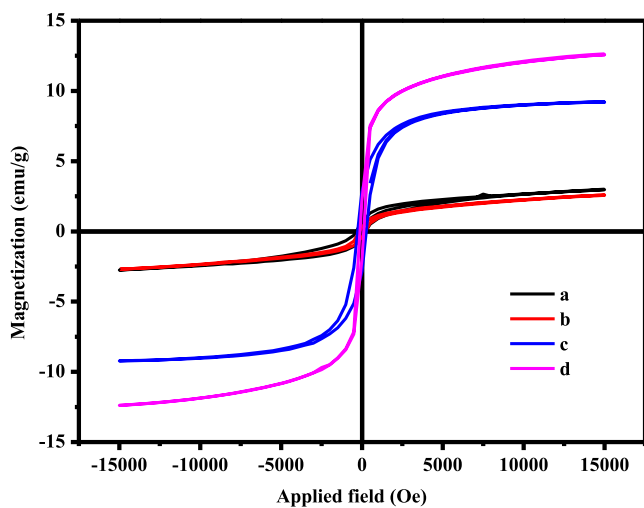$$\sigma_{ac} = \omega \varepsilon_r A \tan \delta \varepsilon_0, \qquad (4)$$
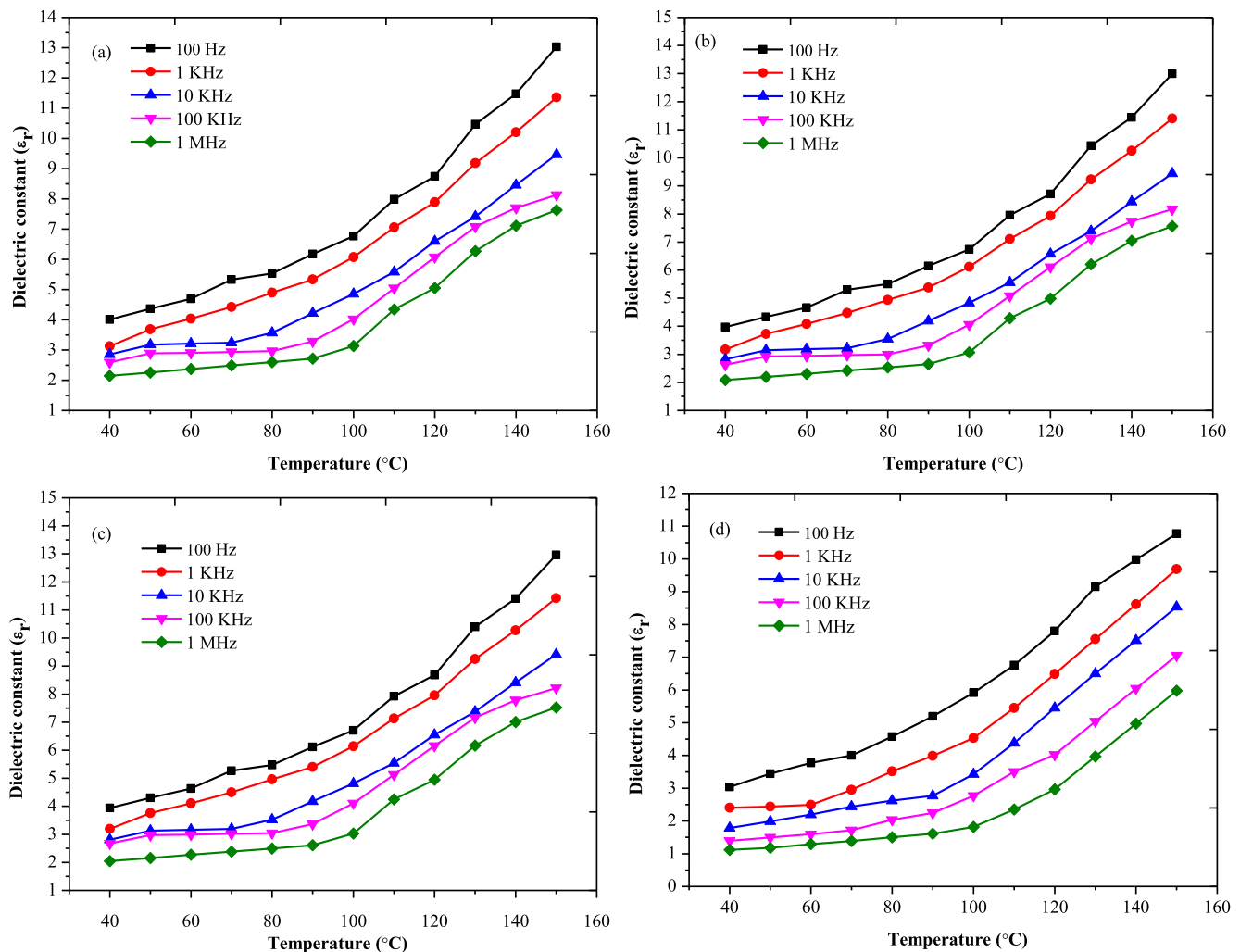
TABLE II. M_s, M_r, and coercivity of $ZnFe_{2-x}Al_xO_4$ (x = 0.0, 0.1, 0.3, and 0.5) samples.

Sample	Sample code	M_s (emu/g)	M_r (emu/g)	Coercivity (Oe)
$ZnFe_2O_4$	a	3.05	0.71	294.75
$ZnFe_{1.9}Al_{0.1}$ Fe_2O_4	b	2.58	0.35	208.97
$ZnFe_{1.7}Al_{0.3}$ Fe_2O_4	c	9.19	2.82	264.22
$ZnFe_{1.5}Al_{0.5}$ Fe_2O_4	d	12.62	2.25	95.22

FIG. 8. Dielectric constant of (a) $ZnFe_2O_4$, (b) $ZnFe_{0.9}Al_{0.1}O_4$, (c) $ZnFe_{0.7}Al_{0.3}O_4$, and (d) $ZnFe_{0.5}Al_{0.5}O_4$ nanoparticles.

where σ_{ac} is the AC electrical conductivity, ω is the angular frequency ($\omega = 2\pi f$, where f is the frequency), ε_0 is the permittivity of free space (8.85×10^{-12} F/m), ε_r is the relative permittivity, A is area of the cross section, and tan δ is the loss tangent. The σ_{ac} vs T graphs of Al-doped $ZnFe_2O_4$ nanoparticles at two distinct temperatures and frequencies (313–423 K and 100 Hz to 1 MHz, respectively) are displayed in Figs. 9(a)–9(d). Each sample has regular dielectric properties, which are distinguished by substantial conductivity at higher frequencies. Because there were fewer open locations at lower temperatures, there was less conductivity, as observed. However, as the temperature increases, so does the quantity of defect sites, which increases the conductivity due to the fact that it has more defects.
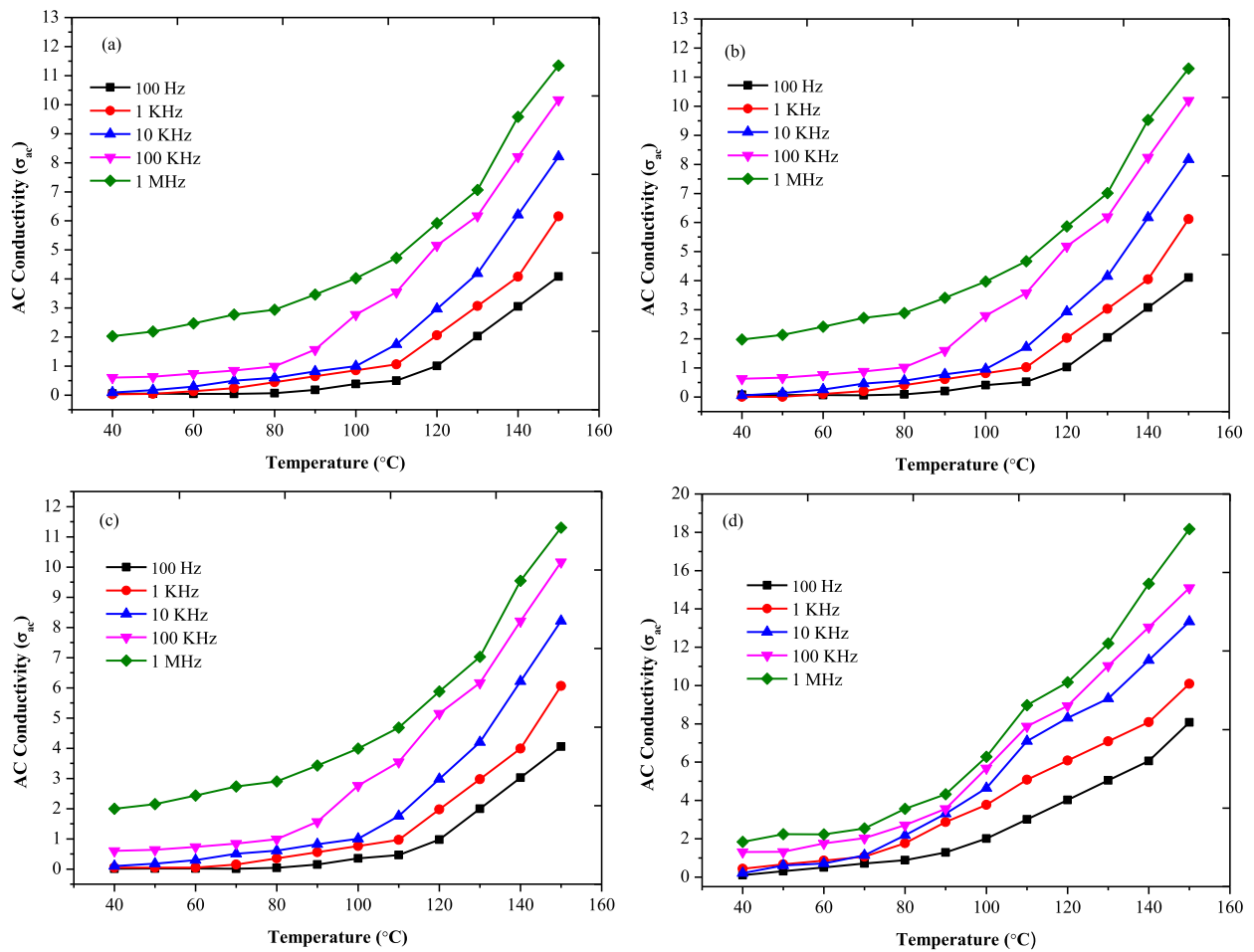
FIG. 9. AC conductivity of (a) $ZnFe_2O_4$, (b) $ZnFe_{0.9}Al_{0.1}O_4$, (c) $ZnFe_{0.7}Al_{0.3}O_4$, and (d) $ZnFe_{0.5}Al_{0.5}O_4$ nanoparticles.

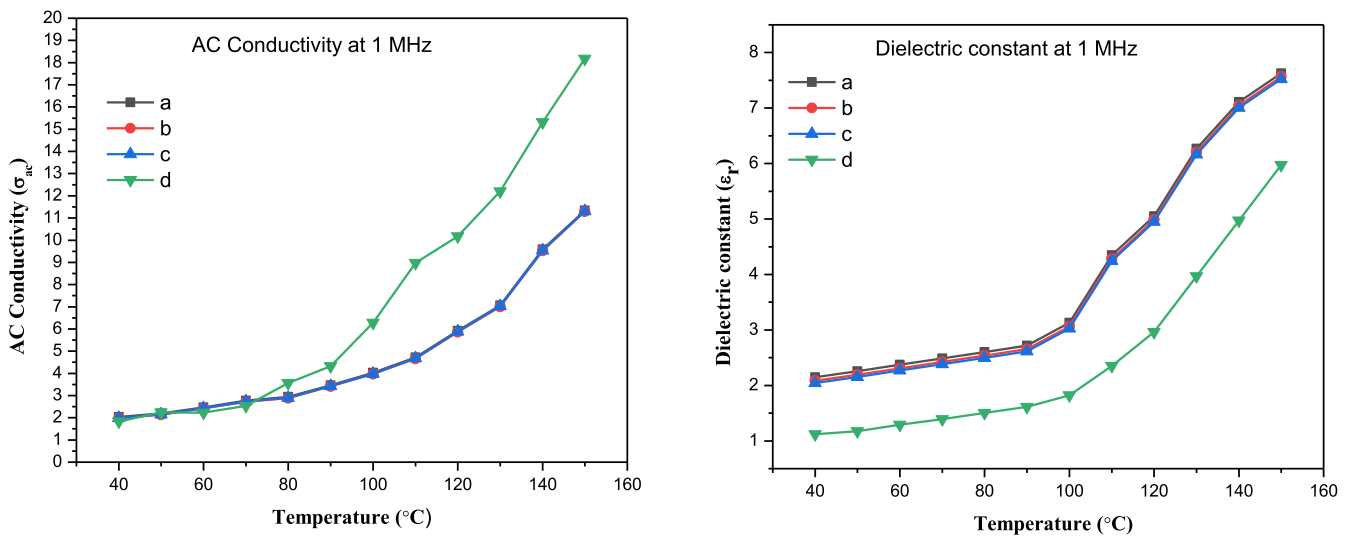**FIG. 10.** AC conductivity and dielectric constant of (a) $ZnFe_2O_4$, (b) $ZnFe_{0.9}Al_{0.1}O_4$, (c) $ZnFe_{0.7}Al_{0.3}O_4$, and (d) $ZnFe_{0.5}Al_{0.5}O_4$ nanoparticles at 1 MHz.
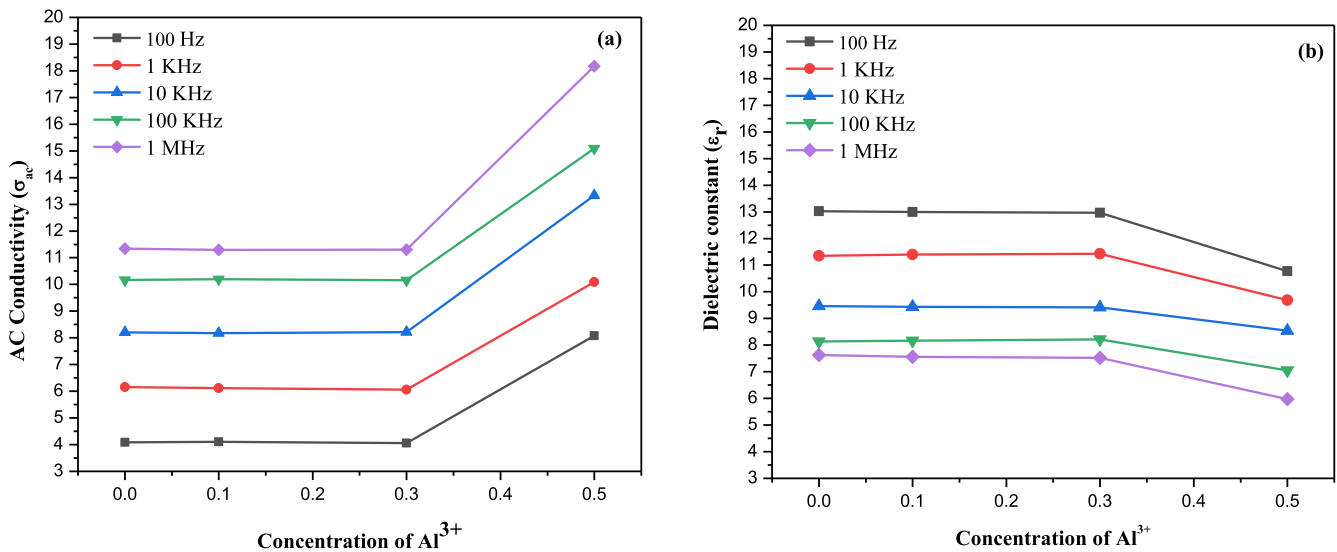
FIG. 11. (a) AC conductivity vs concentration of Al^{3+}. (b) Dielectric constant vs concentration of Al^{3+}.

The permittivity [Eq. (5)] is the product of relative permittivity (dielectric constant) and vacuum dielectric constant (ε_0),

$$\varepsilon = \varepsilon_r \, \varepsilon_0. \qquad (5)$$

Figures 10(a)–10(d) show the dielectric constant and AC conductivity temperature-dependent plots of $ZnFe_{2-x}Al_xO_4$ samples over a range of temperatures and frequencies (313–423 K and 100 Hz to 1 MHz, respectively). Every sample displays robust conductivity and dielectric constant at higher frequencies, indicating typical dielectric properties. Lower temperatures cause a reduction in the number of available sites, resulting in a decrease in conductivity and dielectric constant. With the temperature increase, the creation of defect sites is amplified, resulting in a higher level of conductivity and dielectric constant. From Figs. 11(a) and 11(b), it is evident that the $ZnFe_{1.5}Al_{0.5}O_4$ sample displayed exceptional AC conductivity and low dielectric constant due to a higher concentration of defect sites.[21,22]

IV. CONCLUSIONS

In conclusion, Al doped $ZnFe_2O_4$ ferrites were effectively made by the combustion method and at a temperature of 570 °C. Utilizing x-ray diffraction, every sample has been examined and found to have a crystalline structure in the cubic phase. A diminishing trend is shown by the fluctuation in the lattice parameter with increasing Al doping concentration. The increased Al^{3+} doping concentration causes a progressive increase in the size of the mixed ferrite crystallites. The IR absorption band, which is located between 450, 544, 778, and 1059 cm^{-1}, is associated with the Fe^{3+}–O^{2-} bond's vibration at the tetrahedral (A) site, and Zn^{2+}–O^{2-} are free of any evidence of an impurity peak. Studying the dielectric characteristics of the spinel NPs showed changes as the frequency and temperature varied.

AUTHOR DECLARATIONS

Conflict of Interest

The authors have no conflicts to disclose.

Author Contributions

M. Sundararajan: Data curation (equal); Formal analysis (equal); Methodology (equal); Supervision (equal). **Kholod Dahlous**: Conceptualization (equal); Formal analysis (equal); Methodology (equal). **M. Ramesh**: Software (equal); Writing – original draft (equal). **R. S. Rimal Isaac**: Methodology (equal); Resources (equal); Visualization (equal). **S. Yuvaraj**: Data curation (equal); Formal analysis (equal); Supervision (equal); Writing – review & editing (equal). **Jothi Ramalingam Rajabathar**: Investigation (equal); Methodology (equal); Writing – original draft (equal). **Chandra Sekhar Dash**: Validation (equal); Writing – review & editing (equal). **P. Aji Udhaya**: Methodology (equal); Validation (equal).

DATA AVAILABILITY

The data that support the findings of this study are available from the corresponding author upon reasonable request.

REFERENCES

[1]E. J. W. Verwey and P. W. Haayman, "Electronic conductivity and transition point of magnetite ('Fe$_3$O$_4$')," Physica **8**, 979–987 (1941).

[2] G. A. Sawatzky, J. M. D. Coey, and A. H. Morrish, "Mössbauer study of electron hopping in the octahedral sites of Fe$_3$O$_4$," J. Appl. Phys. **40**, 1402–1403 (1969).

[3] G. A. Petitt and D. W. Forester, "Mössbauer study of cobalt–zinc ferrites," Phys. Rev. B **4**, 3912 (1971).

[4] R. Iyer, R. Desai, and R. V. Upadhyay, "Low temperature synthesis of nanosized Mn$_{1-x}$Zn$_x$Fe$_2$O$_4$ ferrites and their characterizations," Bull. Mater. Sci. **32**, 141–147 (2009).

[5] M. Rozman and M. Drofenik, "Hydrothermal synthesis of manganese zinc ferrites," J. Am. Ceram. Soc. **78**, 2449–2455 (1995).

[6] T. Gonzalez-Carreno, M. P. Morales, M. Gracia, and C. J. Serna, "Preparation of uniform γ-Fe$_2$O$_3$ particles with nanometer size by spray pyrolysis," Mater. Lett. **18**, 151–155 (1993).

[7] S. S. Kumbhar, M. A. Mahadik, V. S. Mohite, K. Y. Rajpure, and C. H. Bhosale, "Synthesis and characterization of spray deposited nickel–zinc ferrite thin films," Energy Proc. **54**, 599–605 (2014).

[8] N. Kaushal, S. Sarraf, A. K. Basu, S. Mishra, and A. Saha, "Facile microwave synthesis of Zinc Ferrite@NCDs for photocatalytic degradation of fluoroquinolone antibiotics," Mater. Chem. Phys. **314**, 128823 (2024).

[9] M. Sundararajan, L. John Kennedy, and J. Judith Vijaya, "Synthesis and characterization of cobalt substituted zinc ferrite nanoparticles by microwave combustion method," J. Nanosci. Nanotechnol. **15**, 6719–6728 (2015).

[10] M. A. Bashar, M. T. H. Molla, D. Chandra, M. D. Malitha, M. S. Islam, M. S. Rahman, and M. S. Ahsan, "Hydrothermal synthesis of cobalt substitute zinc-ferrite (Co$_{1-x}$Zn$_x$Fe$_2$O$_4$) nanodot, functionalised by polyaniline with enhanced photocatalytic activity under visible light irradiation," Heliyon **9**, e15381 (2023).

[11] M. Sundararajan, M. Sukumar, C. S. Dash, A. Sutha, S. Suresh, M. Ubaidullah, A. M. Al-Enizi, M. K. Raza, and D. Kumar, "A comparative study on NiFe$_2$O$_4$ and ZnFe$_2$O$_4$ spinel nanoparticles: Structural, surface chemistry, optical, morphology and magnetic studies," Physica B **644**, 414232 (2022).

[12] M. Sundararajan and L. J. Kennedy, "Photocatalytic removal of rhodamine B under irradiation of visible light using Co$_{1-x}$Cu$_x$Fe$_2$O$_4$ (0≤ x≤ 0.5) nanoparticles," J. Environ. Chem. Eng. **5**, 4075–4092 (2017).

[13] B. Jyothish and J. Jacob, "Al-doped zinc ferrite nanoparticles: Preparation and evaluation of thermal, structural, morphological and anticancer properties," J. Alloys Compd. **863**, 158352 (2021).

[14] S. Yuvaraj, P. Aji Udhaya, S. Deepa, M. Sundararajan, R. Jothiramalingam, H. Al-Lohedan, H. Al-Sigh, and A. A. Nazeer, "Synthesis and Exploring structural, magnetic, morphology and optical properties of La$_{2-x}$Al$_x$CuO$_4$ (0 ≤ x ≤ 0.25) perovskite nanoparticles by microwave-assisted combustion method," J. Ovonic Res. **20**, 143–153 (2024).

[15] N. Vidyarajan and L. K. Alexander, "Strain induced optical properties of perovskite LaFeO$_3$," Mater. Res. Express **6**, 015610 (2018).

[16] M. H. Habibi and H. J. Parhizkar, "FTIR and UV–vis diffuse reflectance spectroscopy studies of the wet chemical (WC) route synthesized nano-structure CoFe$_2$O$_4$ from CoCl$_2$ and FeCl$_3$," Spectrochim. Acta, Part A **127**, 102–106 (2014).

[17] S. Revathi, R. Srimathi, A. Kumar, J. Kaur, S. Yuvaraj, M. Ubaidullah, M. Sundararajan et al., "Monitoring the effect of In^{3+} doping on the structural, morphological, optical, vibrational, and magnetic properties of perovskite LaFeO$_3$ nanoparticles," Inorg. Chem. Commun. **168**, 112777 (2024).

[18] D. Zhang, A. B. Karki, D. Rutman, D. P. Young, A. Wang, D. Cocke, T. H. Ho, and Z. Guo, "Electrospun polyacrylonitrile nanocomposite fibers reinforced with Fe$_3$O$_4$ nanoparticles: Fabrication and property analysis," Polymer **50**, 4189–4198 (2009).

[19] L. Kumar and M. Kar, "Influence of Al^{3+} ion concentration on the crystal structure and magnetic anisotropy of nanocrystalline spinel cobalt ferrite," J. Magn. Magn. Mater. **323**, 2042–2048 (2011).

[20] K. Mathankumar, M. Sukumar, C. S. Dash, M. Sundararajan, M. Ubaidullah, A. M. Al-Enizi, A. Sutha, M. Kausar Raza, J. Arockia Dhanraj, and D. Kumar, "Facile synthesis, characterization, catalytic and photocatalytic activity of multiferroic BiFeO$_3$ perovskite nanoparticles," J. Inorg. Organomet. Polym. Mater. **32**, 3476–3487 (2022).

[21] A. Dennis Raj, M. Jeeva, R. Purusothaman, G. Venkatesa Prabhu, M. Vimalan, and I. Vetha Potheher, J. Mater. Sci.: Mater. Electron. **28**, 7802–7810 (2017).

[22] A. Vinosha, J. Emima, K. Raja, A. C. Fernandez, S. Krishnan, A. C. Fernandez et al., "Investigation of optical, electrical and magnetic properties of cobalt ferrite nanoparticles by naive co-precipitation technique," Optik **127**, 9917–9925 (2016).